

TABLE OF CONTENTS

Table of Contents	i
	Page
1 Introduction	1
1.1 Physics	1
1.2 CMS Detector	1
2 Charmonia	3
2.1 Theory	3
2.2 Analysis	3
2.3 Results	3
3 W BOSON PRODUCTION IN PROTON-LEAD COLLISIONS	5
3.1 Theory	6
3.1.1 History of weak theory	6
3.1.2 Electroweak theory	9
3.1.3 Hadron collisions at the LHC	11
3.1.4 PDF global fits	15
3.1.5 Production of W bosons at LHC	19
3.2 W boson production in pPb collisions at $\sqrt{s_{\text{NN}}} = 8.16$ TeV	22
3.2.1 Observables	22
3.2.2 Comparison with theoretical models	24
3.2.3 Comparison with other LHC experiments	26
4 Conclusion	29
Bibliography	31
List of Tables	37

TABLE OF CONTENTS

List of Figures	39
------------------------	-----------

INTRODUCTION

This chapter
BlaBla

1.1 Physics**1.2 CMS Detector**

This chapter
BlaBla

2.1 Theory

2.2 Analysis

2.3 Results

W BOSON PRODUCTION IN PROTON-LEAD COLLISIONS

This chapter describes the measurement of the production of W bosons in proton-lead (pPb) collisions at a nucleon-nucleon center-of-mass energy $\sqrt{s_{\text{NN}}} = 8.16$ TeV with the CMS detector. As mentioned in Section 1.1, the primary processes that contribute at LHC energies to the production of W bosons are $u\bar{d} \rightarrow W^+$ and $d\bar{u} \rightarrow W^-$. Once produced, W bosons can decay weakly to either leptons or quarks. The semi-muonic decay ($W \rightarrow \mu\nu_\mu$) is of particular interest, since muons lose negligible energy in the medium and the surrounding background is small.

The individual W^+ and W^- production rates are expected to be modified relative to proton-proton (pp) collisions, due to the different content of up and down quarks in the proton compared to the lead nuclei. The distribution of partons inside the nuclei can also be modified by parton shadowing (or depletion), which can alter the W boson yields at the LHC. Precise measurements of W production in pPb collisions can therefore provide strong constraints to the nuclear parton distribution functions (nPDF).

The analysis is currently being reviewed. Previous results have been published by the CMS collaboration on pPb data at $\sqrt{s_{\text{NN}}} = 5.02$ TeV collected in 2013 [1]. A similar study has been performed by the ALICE [2] and the ATLAS [3] collaborations at pPb collision energies of 5.02 TeV.

The datasets and simulated samples are described in Section ???. In Section ??, the event selection is presented. The relevant backgrounds are introduced in Section ??.

23 Finally, the systematic uncertainties are discussed in Section ?? and the results are
 24 detailed in Section 3.2.

25 3.1 Theory

26 INTRO PARRAGRAPH MISSING

27 3.1.1 History of weak theory

28 In the early 20th century, quantum mechanics was the standard framework of atomic
 29 physics but certain processes such as the β decay, discovered by Ernest Rutherford in
 30 1899 [4], were not fully understood yet. At the time, the β decay was characterized by
 31 the process $A_i \rightarrow A_f + e^-$, where an initial nucleus A_i decays into another nucleus A_f
 32 emitting an electron during the process. In order to conserve energy, the electron is
 33 required to have a fixed kinetic energy, but James Chadwick observed in 1914 that the β
 34 rays produced a continuous energy spectrum [5, 6] in disagreement with was expected. As
 35 a way to solve the problem of the continuous β decay spectrum, Wolfgang Pauli proposed
 36 in 1930 the existence of a new particle [7, 8]. Pauli named his particle initially the
 37 neutron but later renamed it to the neutrino after the discovery of a new electrically
 38 neutral particle inside the ${}^{14}_7\text{Ni}$ nucleus by Chadwick in 1932 [9]. Pauli described the
 39 neutrino as a neutral fermion with mass close to zero and spin 1/2 capable of penetrating
 40 matter deeper than photons [7].

41 Enrico Fermi, after attending the 7th Solvay conference where the discovery of the
 42 neutron as well as Pauli's neutrino were presented, proposed a new theory to explain
 43 the β decay [10]. Fermi's theory defined the β decay as a process in which the neutron
 44 decays to a proton, emitting an electron and a neutrino. Fermi formulated his theory
 45 using an analogous approach as in Quantum Electrodynamics (QED) by proposing the
 46 following lagrangian for β decay [11]:

$$L_\beta = G_F (\bar{u}_p \gamma_\mu u_n) (\bar{u}_e \gamma^\mu u_\nu) \quad (3.1)$$

47 where u is the Dirac spinor of each particle, γ_μ is the Dirac matrix and G_F is the Fermi
 48 coupling constant. Fermi's theory of weak interactions assumed the same conservation
 49 rules as QED, including the symmetry under reflection in space [11]. A system that is
 50 invariant under reflections conserve a quantity called parity which includes an intrinsic

component called spin and a spatial component depending on the angular momentum of the particle.

In the upcoming years, the physicists Tsung Dao Lee and Chen Ning Yang started to doubt the conservation of weak parity after not finding any experimental evidence so far [12]. In an attempt to test the conservation of parity in weak interactions, Lee and Yang proposed in 1956 to study the β decays of Cobalt (^{60}Co) and measure the projection of the momentum of electrons along the spin axis of the Cobalt nucleus [12]. If the decay process conserves parity then electrons would be produced in all directions. The experiment to test the conservation of weak parity was realized by Chien-Shiung Wu in 1957. The results of Wu's research showed that electrons were preferentially produced in the opposite direction to the Cobalt spin [13], which meant that parity was not conserved in weak interactions.

Apart from parity, one can also associate a helicity to particles. The particle's helicity is considered right-handed if the direction of the particle's momentum and spin are the same, and left-handed otherwise. In 1958, Goldhaber, Grodzins and Sunyar measured the neutrino helicity at Brookhaven National Laboratory (BNL) and discovered that neutrinos were always left-handed and antineutrinos were right-handed [14]. As a consequence of the discovery of parity violation and the neutrino helicity, Lee and Yang modified Fermi's weak theory and introduced an axial vector term, giving rise to the V-A (vector-axial) theory of weak interactions. Even though parity (P) and charge conjugation (C) (transforms particles into their antiparticles) were violated separately, it was assumed that the combined CP operation was still conserved by the weak force.

The assumption of the conservation of CP did not last long. An experiment performed at BNL by James Christenson, James Cronin, Val Fitch and Rene Turlay [15] in 1964 concluded that the long-lived K_L meson ($\text{CP}=-1$) was able to decay to two pions ($\text{CP}=+1$) violating CP in the process. To explain the CP violation in weak theory, Makoto Kobayashi and Toshihide Maskawa [16] extended the formulation of the Cabibbo matrix to include three generation of quarks and a CP-violating phase term. The Cabibbo matrix was originally computed by Nicola Cabibbo [17] including four quarks to explain the different amplitudes observed between the up, down and strange quark transitions. The development of the Cabibbo, Kobayashi and Maskawa (CKM) matrix led to the prediction of the bottom and top quarks, discovered later in 1977 [18] and 1995 [19], respectively.

Following Paul Dirac's formulation of QED [20], Sheldon Glashow [21], Steven Weinberg [22] and Abdus Salam [23] managed in 1968 to build a gauge-invariant unified theory of the electromagnetic and weak interactions, for which they were awarded the

Nobel Prize in Physics in 1979 [24]. In order to make the electroweak theory symmetric under local phase transformations, it required the presence of four spin-1 massless bosons: two electrically charged particles called W^\pm bosons and two neutral particles corresponding to the Z boson and photon. But since weak interactions are short range, the weak force has to be mediated by massive bosons. The addition of mass to the bosons was realized after introducing the spontaneous local breaking of the underlying SU(2) symmetry through the Higgs mechanism [25, 26]. In the following years, Gerardus't Hooft and Martinus Veltman managed to renormalize the electroweak theory [27, 28], allowing to calculate more precisely the theoretical masses of the weak bosons.

The experimental study of weak bosons would require the development of new particle acceleration technologies. In 1976, Carlo Rubbia, Peter McIntyre and David Cline suggested to transform CERN's circular proton accelerator called Super Proton Synchrotron (SPS) into a proton-antiproton collider (Sp \bar{p} S) [29]. The upgrade to Sp \bar{p} S was made possible thanks to the stochastic cooling technology invented by Simon Van der Meer [30] in 1972, which allowed to cool down and collect antiprotons. Several experiments, named Underground Area (UA), were built to study the proton-antiproton collisions at the Sp \bar{p} S. The UA1 and UA2 collaborations discovered the W boson [31, 32] in 1983 after reporting the observation of electrons with large transverse energy and the presence of missing energy in $p\bar{p}$ collisions at $\sqrt{s} = 540$ GeV. And few months later, both collaborations also reported the discovery of the Z boson in the dilepton decay channel [33, 34]. These outstanding discoveries convinced the Swedish Academy of Science to award in 1984 the Nobel Prize in Physics to Rubbia and Van der Meer for their contributions to the Sp \bar{p} S program [35].

After the major success of the Sp \bar{p} S project, CERN constructed in 1983 a new lepton circular collider called the Large Electron-Positron (LEP) collider [36]. LEP was designed to accelerate electrons and positrons to an energy of half the Z boson mass (45 GeV) in order to perform precision measurements of the Z boson lineshape. Furthermore, a precise measurements of the W mass [37] was later performed by the experiments in the Fermi National Accelerator Laboratory (FNAL). The FNAL analyzed data collected between 1983 and 2011 from the Tevatron [38], a proton-antiproton synchrotron collider that operated at energies up to 1 TeV.

The succesful programs of LEP and Tevatron produced the most precise measurements of the properties of the electroweak theory, but there was still a missing piece to complete the picture, the Higgs boson. The discovery of the Higgs boson was finally achieved in 2012 by the CMS [39] and ATLAS [40] collaborations at the Large Hadron

121 Collider (LHC).

122 3.1.2 Electroweak theory

123 The interactions between elementary particles mediated by the weak and electromagnetic
 124 forces are described in the Standard Model using the electroweak theory developed by
 125 Glashow, Weinberg and Salam [21–23]. The unification of these two fundamental forces
 126 of nature is accomplished mathematically using a non-abelian $SU(2) \times U(1)_Y$ gauge
 127 theory. The electroweak theory requires four massless gauge bosons: three bosons with
 128 weak isospin (called W_1 , W_2 and W_3) from $SU(2)$ and one boson (named B) with weak
 129 hypercharge from $U(1)_Y$.

130 Since weak bosons have mass, a full description of the electroweak interactions
 131 requires the inclusion of massive vector bosons. The problem is that one can not naively
 132 add a mass term of the form $m^2 W^\mu W_\mu$ into the electroweak lagrangian since this would
 133 break gauge invariance making the theory divergent. Thus, this issue is instead solved
 134 by spontaneously breaking the $SU(2) \times U(1)_Y$ electroweak symmetry into a $U(1)_{EM}$
 135 symmetry using the Higgs mechanism [25, 26]. The overall idea is that the electroweak
 136 gauge bosons couple to a scalar field called the Higgs field which is present in all space.
 137 When the Higgs field induces a spontaneous breaking of the gauge symmetry, the Higgs
 138 field is splitted into one dynamic part corresponding to the Higgs boson, and another
 139 constant part called the vacuum expectation value (VEV). The symmetry breaking of
 140 $SU(2) \times U(1)_Y$ to $U(1)_{em}$ generates three massless Goldstone bosons. The goldstone
 141 bosons are then absorbed by the electroweak gauge bosons producing the W^+ , W^- and Z
 142 bosons with masses proportional to the VEV, while the photon remains massless. The W^\pm ,
 143 Z and γ bosons are correlated with the W_1, W_2, W_3 and B gauge bosons in the following
 144 way:

$$\begin{aligned} W^\pm &= \frac{1}{\sqrt{2}}(W_1 \pm W_2) \\ \begin{pmatrix} Z \\ \gamma \end{pmatrix} &= \begin{pmatrix} \cos\theta_W & \sin\theta_W \\ -\sin\theta_W & \cos\theta_W \end{pmatrix} \begin{pmatrix} B \\ W_3 \end{pmatrix} \end{aligned} \quad (3.2)$$

145 where θ_W represents the weak mixing angle. In addition, the quarks acquire mass
 146 through the Yukawa interaction with the Higgs field. Since the quark weak eigenstates
 147 are not the same as their mass eigenstates, weak interactions can induce a transition
 148 from a up-like quark (u, c, t) to a down-like quark (d, s, b). The strength of the quark
 149 flavour mixing in weak decays is parameterized by the CKM matrix V_{CKM} via:

$$\begin{pmatrix} d' \\ s' \\ b' \end{pmatrix} = \begin{pmatrix} V_{ud} & V_{us} & V_{ub} \\ V_{cd} & V_{cs} & V_{cb} \\ V_{td} & V_{ts} & V_{tb} \end{pmatrix} \begin{pmatrix} d \\ s \\ b \end{pmatrix} \quad (3.3)$$

150 where (d', s', b') are the down-like quark weak eigenstates and (d, s, b) are the
151 corresponding mass eigenstates. The latest values of the CKM matrix elements are [41]:

$$V^{\text{CKM}} = \begin{pmatrix} 0.97417 & 0.2248 & 0.00409 \\ 0.220 & 0.995 & 0.0405 \\ 0.0082 & 0.04 & 1.009 \end{pmatrix} \quad (3.4)$$

152 The lagrangian of the electroweak theory includes several components that describes
153 the interactions between the fermions, electroweak bosons and the Higgs boson. In the
154 case of the Z boson, the term of the lagrangian that represents the interactions between
155 fermions and neutral charged electroweak bosons is:

$$L_{NC} = \alpha_{em} \theta_W \sum_{\text{fermions}} \bar{f} \gamma^\mu A_\mu f + \frac{g}{\cos \theta_W} \sum_{\text{fermions}} \bar{f} \gamma^\mu \frac{(g_v^f - g_a^f \gamma^5)}{2} Z_\mu f \quad (3.5)$$

156 where g is the coupling constant of $SU(2)_L$, f is the Dirac spinors of fermions, A_μ
157 is the electromagnetic field, and g_v^f (g_a^f) is the fermion vector (axial) weak coupling
158 constants. Eq. (3.5) specify that the Z bosons and photons conserve flavour always
159 decaying into a fermion and its corresponding antifermion. Even though photons do
160 not distinguish the helicity of particles, the Z boson couplings are different for left- and
161 right-handed fermions.

162 Furthermore, the component of the lagrangian that represents the interaction be-
163 tween the W bosons and the fermions is given by:

$$L_{CC} = \frac{g}{2\sqrt{2}} \left((\bar{u}, \bar{c}, \bar{t})_R W_\mu^+ \gamma^\mu V^{\text{CKM}} \begin{pmatrix} d_L \\ s_L \\ b_L \end{pmatrix} + (\bar{\nu}_e, \bar{\nu}_\mu, \bar{\nu}_\tau)_R W_\mu^+ \gamma^\mu \begin{pmatrix} e_L^- \\ \mu_L^- \\ \tau_L^- \end{pmatrix} \right) \quad (3.6)$$

164 where f_L correspond to left-handed fermions and \bar{f}_R represents right-handed an-
165 tifermsions. Thus, W bosons only couple to right-handed antifermions and left-handed
166 fermions organized in pairs of lepton-neutrino or quark-antiquark, where the electric
167 charge of the of particles differ by one unit. Since the top quark mass (178 GeV) is larger
168 than the W boson mass (80 GeV), the W boson can not decay to a top quark. Fig. 3.1

shows the possible decays of W bosons to fermions. The measured values of the mass, width and couplings of weak vector bosons are summarized in Table 3.1.2.

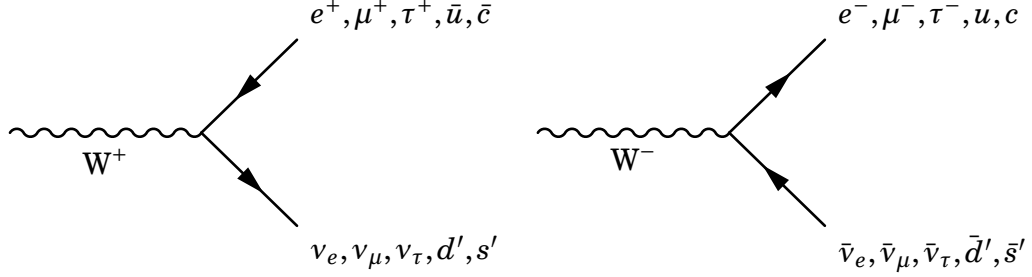


Figure 3.1: Feynman diagram of the decay modes of W^+ (left) and W^- (right) bosons to fermions.

Variable	Description	Value
M_W	W boson mass	80.385 ± 0.015 GeV
Γ_W	W boson width	2.085 ± 0.042 GeV
$\text{BR}(W \rightarrow \ell \nu)$	Branching fraction of W boson semileptonic decays	$(10.86 \pm 0.09)\%$
$\text{BR}(W \rightarrow q \bar{q}')$	Branching fraction of W boson hadronic decays	$(67.41 \pm 0.27)\%$
M_Z	Z boson mass	91.1876 ± 0.0021 GeV
Γ_Z	Z boson width	2.4952 ± 0.0023 GeV
$\text{BR}(Z \rightarrow \ell^+ \ell^-)$	Branching fraction of Z boson charged-lepton decays	$(3.3658 \pm 0.0023)\%$
$\text{BR}(Z \rightarrow \nu \bar{\nu})$	Branching fraction of Z boson neutrino decays	$(20.00 \pm 0.06)\%$
$\text{BR}(Z \rightarrow q \bar{q})$	Branching fraction of Z boson hadronic decays	$(69.91 \pm 0.06)\%$

Table 3.1: Experimental values of the mass, width and branching fractions of weak bosons extracted from the PDG [41].

3.1.3 Hadron collisions at the LHC

Hadrons are not elementary particles due to their internal structure composed of partons (i.e. quarks and gluons). The production of particles in hadronic collisions depends on the evolution of the partons inside the hadrons and the parton momentum transfer during the hard scattering. In this thesis, the production of W bosons is determined from collisions of protons against Lead ions (pPb), so we need to take into account the interplay between protons and Pb nuclei.

Protons can be described as a collection of three valence quarks: one down quark and two up quarks. The quantum properties of the proton, such as the electric charge or spin,

are derived from the valence quarks. The interaction between valence quarks is mediated by the exchange of gluons. Gluons inside the hadrons can also produce quark-antiquark pairs and other gluons through self interactions. The quark-antiquark pairs produced inside the hadron are called sea quarks and only exist virtually. The gluons and sea quarks do not contribute to the quantum numbers of hadrons but they play a key role in the interaction of hadrons with other particles.

Since the strength of the strong interactions decreases with energy, the partons can be considered effectively free within the proton during high energy collisions. In this case, each parton carries a fraction of the proton's total momentum, represented by the quantity called Bjorken x [42] (labelled simply as x), given by:

$$p_{parton} = x p_{proton} \quad (3.7)$$

The parton distribution functions (PDF) describes the probability that a parton carries a given fraction of the proton's momentum. The PDFs can not be currently calculated due to the nonperturbative nature of QCD, but they can be constrained from fits to experimental data due to the factorization theorem.

The factorization theorem indicates that the cross section of a given process in hadronic collisions can be factorized, in all orders of the perturbative expansion, into a partonic cross section and the nonperturbative PDFs of the incoming hadrons. The partonic cross section can be derived using perturbative QCD regardless of the incoming hadron while the PDFs can be determined from global fits to the data since they are universal (i.e. the PDFs are independent of the initial process). The hadronic cross section in a given final state can be expressed at leading order, using the factorization theorem, as:

$$\sigma_{h1,h2} = \sum_{f1,f2=(q,\bar{q},g)} \int_0^1 dx_1 dx_2 f_1^{h1}(x_1, Q^2) f_2^{h2}(x_2, Q^2) \hat{\sigma}_{f1f2} \quad (3.8)$$

where Q^2 is the momentum scale, $f(x, Q^2)$ is the PDF, and $\hat{\sigma}$ represents the partonic cross section. The Q^2 scale dependence of the PDFs is described by the parton evolution equations developed by Dokshitzer, Gribov, Lipatov, Altarelli and Parisi (DGLAP) [43–45].

In the DGLAP formalism, the PDFs can be expressed in terms of kernels P_{q1q2} (called splitting functions), and the evolution equations of the quark q and gluon g densities can be written as:

$$\begin{aligned}
\frac{d}{dt}q_i(x,t) &= \frac{\alpha_s(Q)}{2\pi} [q_i \otimes P_{qq} + g_i \otimes P_{qg}] \\
\frac{d}{dt}g(x,t) &= \frac{\alpha_s(Q)}{2\pi} \left[\sum_i (q_i + \bar{q}_i) \otimes P_{gq} + g_i \otimes P_{gg} \right] \\
[q \otimes P] &= \int_x^1 d\epsilon \frac{(q(\epsilon, t))}{\epsilon} \times P\left(\frac{x}{\epsilon}\right)
\end{aligned} \tag{3.9}$$

where $t \propto \text{Log}(Q^2)$, and $P_{q_1 q_2}$ is the probability of finding a parton q_1 in another parton q_2 . In other words, the DGLAP evolution equations state that the PDF of a given parton q at an x value is determined from the contribution of all the partons at higher momentum fraction considering their probability of decaying into the parton q .

From the definition of the PDFs, one can also formulate a set of structure functions defined as:

$$F_2^p(x) = \sum_f e_f^2 f(x, Q^2) x \tag{3.10}$$

where e_f is the electric charge of a given fermion f . The structure functions were extensively measured in Deep-Inelastic Scattering (DIS) collisions at the Hadron-Elektron-Ringanlage (HERA) accelerator by the ZEUS and H1 collaborations. The measurements of the F_2 structure function performed by the ZEUS collaboration [46] at HERA are shown in Fig. 3.2.

The DIS process consists in the inelastic scattering of electrons off protons as presented in Fig. 3.3. In the DIS process, the momentum transferred from the electron to the proton is defined as $Q^2 = -q^2 = -(k - k')^2$ and the corresponding Bjorken x fraction is $x = Q^2/2(p_{in} \cdot q)$. Even though DIS experiments were not able to probe the gluons directly, the DIS data showed that valence quarks did only carry half of the proton momentum been the rest carried by the gluons.

Another important process that takes place in hadron colliders is the Drell-Yan (DY) production. In the DY process a quark from one hadron and an antiquark from another hadron annihilate into a virtual photon (γ^*) or Z boson which then decays to a pair of leptons as shown in Fig. 3.4. Drell-Yan production is used to constrain the quark PDFs in a wide range of momentum fraction x depending on the invariant mass of the dilepton pair. In addition, the Drell-Yan process also contributes to the background of the W boson production when one the DY final state leptons is generated outside of the detector acceptance.

We have considered until now only the structure of protons, but the nuclear environment of ions can also impact the production of particles. Pb ions are composed of 82

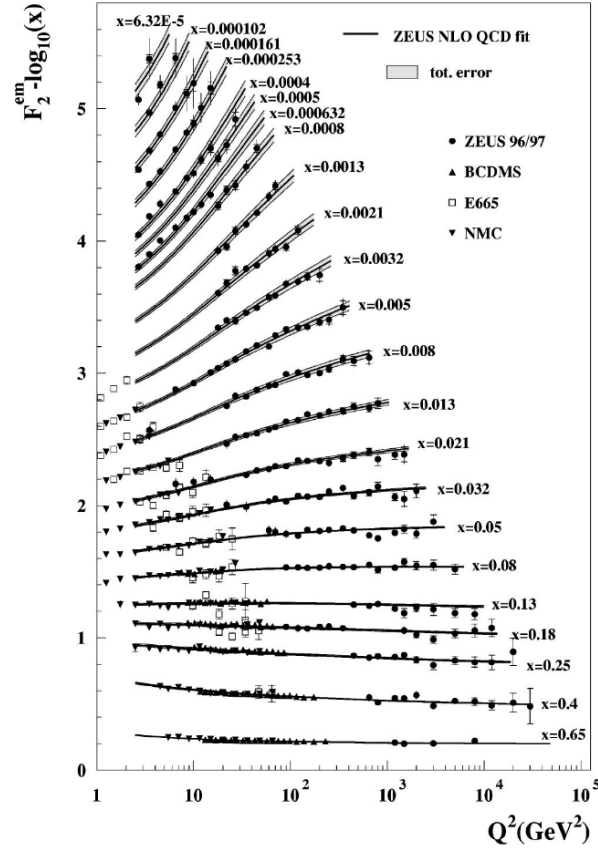


Figure 3.2: NLO QCD fits to the to the ZEUS F_2 structure function data from 1996, 1997 and proton fixed-target at HERA. The error bands of the fit represent the total experimental uncertainty from both correlated and uncorrelated sources. Figure taken from Ref. [46]

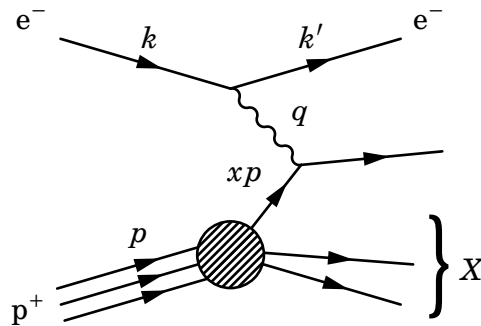


Figure 3.3: Feynman diagram of deep inelastic scattering of electrons against protons

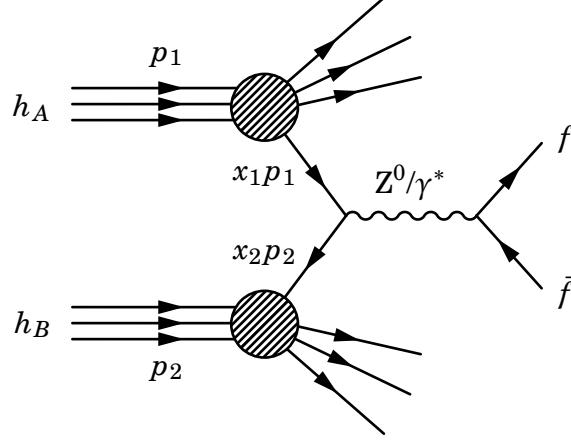


Figure 3.4: Feynman diagram of neutral charged Drell-Yan process

protons and 126 neutrons. The neutron PDF can be derived from the proton PDF using isospin symmetry (i.e. by exchanging the up and down quark PDFs), while assuming the same gluon PDF as in the proton. If no nuclear modifications are expected, protons and neutrons should then behave as free particles inside the nucleus, and one could simply sum the PDFs of the protons and neutrons scaled accordingly. In this case, the ratio of the PDF of protons bounded in the nucleus (nuclear PDF) over the free-proton PDF should be one.

To determine the nuclear modifications, the heavy ion measurements were first compared to results using deuterium. The European Muon Collaboration (EMC) measured the structure function of DIS in iron and deuterium targets between 1977 and 1988, and observed a depletion of the iron PDFs relative to the deuterium PDFs at $x > 0.2$ (EMC region) [47] and at $x < 0.01$ (shadowing region) [48]. Subsequent results found an enhancement at the intermediate region $0.01 < x < 0.2$ (antishadowing region) [49]. Since current heavy ion data is more limited than data from proton collisions, the global fits of the nuclear PDFs are less accurate than the proton PDFs.

3.1.4 PDF global fits

The parton distribution functions can not be currently determined from first principles due to the nonperturbative behaviour of the strong interactions. Nevertheless, their dependence on x can be derived by fitting observables (e.g. structure functions or asymmetries) to experimental data from different processes since PDFs do not depend on the

initial hard scattering. The Q^2 dependence of the PDFs is determined using the DGLAP evolution equations. The most common processes used to constrain the PDFs correspond to Drell-Yan, DIS, vector boson and jet production, which have been measured by various experiments including data from HERA, SLAC and LHC.

There are several proton PDFs currently available. One of the most commonly used proton PDF in high energy physics nowadays is the one provided by the Collaboration of Theorists and Experimentalist (CTEQ). The most recent CTEQ PDF corresponds to CT14 published in 2016 [50]. The global fits of CT14 PDFs include data of vector bosons and jets from LHC pp collisions at 7 TeV and 8 TeV, charm quark DIS production from HERA, and electron charge asymmetry from Tevatron. The x -dependence of the CT14 PDF is parameterized at low Q^2 scale by [50]:

$$xf_a(x, Q^2) = x^{c_1} (1-x)^{c_2} P_a(x) \quad (3.11)$$

where P_a is a polynomial with different parameters for each parton. In the case of the up and down valence quarks, P_a is expressed as a Bernstein polynomial of fourth-order in \sqrt{x} . The P_a distribution of gluon and the light sea quark PDFs is given instead by a Bernstein polynomial in $y = (2\sqrt{x} - x)$ of second-order and fourth-order, respectively. There is not enough data to constrain the strange quark and antiquark PDFs so they are assumed to be equal. In total, the CT14 PDFs are described by 26 fitting parameters including: 8 parameters for the valence quarks, 5 parameters for the gluon and 13 parameters for the sea quarks [50].

The first global fit to describe leading-order nuclear effects was the EKS98 nPDF [51]. The pion data collected by RHIC was later included in EPS08 [52], EPS09 [53], DSSZ [54] and nCTEQ15 [55] nPDFs which provided constraints to the gluon nPDF. We will focus on the latest nuclear PDF calculations which are the EPPS16 [56] and the nCTEQ15 [55] NLO nPDFs.

The EPPS16 nPDFs [56] are derived from a global analysis of nuclear data sets published in 2017 by the group of Eskola, Paakkinen, Paukkunen and Salgado (EPPS). The EPPS16 nPDF calculations updates their previous EPS09 [53] global fits. EPPS16 includes five additional parameters compared to EPS09 to account for possible flavour dependence of the quark nuclear modifications. The EPPS16 global fits includes the same data sets as EPS09 (charged-lepton-nucleus DIS data from SLAC, DY dilepton production from EMC proton-nucleus collisions and inclusive pion production from RHIC deuteron-nucleus collisions), as well as the CHORUS neutrino-nucleus DIS data, low-mass DY production from RHIC pion-nucleus collisions, and the results using dijet and

electroweak boson production in LHC pPb collisions at $\sqrt{s_{\text{NN}}} = 5.02$ TeV. The addition of the new LHC, RHIC and CHORUS data into the global fit is not in tension with the previous EPS09 data sets, reassuring the validity of the universality of the nPDFs. Moreover, the inclusion of the CMS measurements of dijet production in pPb collisions at $\sqrt{s_{\text{NN}}} = 5.02$ TeV highly constrained the gluon nPDF. On the other hand, the LHC measurements of the electroweak boson production in pPb data was not able to further constrain the quark nPDF due to the limited statistical precision. The nuclear PDFs are parameterized in EPPS16 as:

$$f_i^{p/A}(x, Q^2) = R_i^A(x, Q^2) f_i^p(x, Q^2) \quad (3.12)$$

where $f_i^{p/A}$ represents the PDF of a proton bounded in a nucleus A, f_i^p is the free proton PDF and R_i^A is the corresponding nuclear modification. The EPPS16 nuclear modifications are derived using the NLO CT14 PDF as the free proton baseline. The parameters of R_i^A are determined in three regions: the shadowing region $x \rightarrow 0$, the antishadowing maximum point x_a and the EMC minimum point x_e . The dependence on the atomic mass A is parameterized along the three x regions in the following way:

$$R_i^A(x, Q_0^2) = R_i^{A_{\text{ref}}}(x, Q_0^2) \left(\frac{A}{A_{\text{ref}}} \right)^{\gamma_i [R_i^{A_{\text{ref}}}(x, Q_0^2) - 1]} \quad (3.13)$$

where Q_0 is the parameterization scale fixed at the charm pole mass (1.3 GeV), γ_i is a positive parameter and $A_{\text{ref}} = 12$. The Q^2 dependence above Q_0^2 is determined by solving the DGLAP parton evolution equations. The strong coupling constant evaluated at the Z boson mass is set to $\alpha_s(M_Z) = 0.118$. The EPPS16 nuclear modifications are parameterized in total by 20 parameters.

The nCTEQ15 nuclear PDF published by Kovarik et al. in 2016 was derived using the CTEQ framework at next-to-leading order. The nCTEQ15 nPDF global fits make use of charged-lepton DIS data, DY dilepton production and RHIC inclusive pion production. In contrast with EPPS16 where the nuclear modification factor $R_i^{p/A}$ is fitted, the nCTEQ15 global analysis parametrizes the nuclear PDF $f_i^{p/A}$ directly (i.e. no free proton PDF is used as baseline). The nCTEQ nPDFs are parameterized as:

$$\begin{aligned} x f_i^{p/A}(x, Q_0) &= c_0 x^{c_1} (1-x)^{c_2} e^{c_3 x} (1 + e^{x_4 x})^{c_5} \\ \frac{\bar{d}(x, Q_0)}{\bar{u}(x, Q_0)} &= c_0 x^{c_1} (1-x)^{c_2} + (1 + c_3 x)(1-x)^{c_4} \\ s^{p/A}(x, Q_0) &= \bar{s}^{p/A}(x, Q_0) = \frac{\kappa(A)}{2} \left(\bar{u}^{p/A}(x, Q_0) + \bar{d}^{p/A}(x, Q_0) \right) \end{aligned} \quad (3.14)$$

314 where $f_i^{p/A}$ is defined for $i = (u_v, d_v, g, \bar{u} + \bar{d}, s + \bar{s}, s - \bar{s})$, $\kappa(A) = (c_{0,0}^{s+\bar{s}} + c_{0,1}^{s+\bar{s}} (1 - A^{-c_{0,2}^{s+\bar{s}}}))$
 315 and the parameterization scale $Q_0 = 1.3$ GeV. The A-dependence of the nCTEQ15 nPDF
 316 is parameterized directly in the coefficients using $c_k(A) = c_{k,0} + c_{k,1}(1 - A^{-c_{k,2}})$, where
 317 $k = 1, \dots, 5$.

318 The nCTEQ15 global fits to the data sets are performed by minimizing the χ^2 . The
 319 nCTEQ15 fits are performed using 16 free parameters separated in: 7 gluon, 4 up valence
 320 quark, 3 down valence quark and 2 ($d + u$) antiquark parameters. Also, nCTEQ15 treat
 321 the light valence quark densities independently but it assume no flavour dependence of
 322 the light antiquark nuclear modifications. The nCTEQ15 calculations avoid fitting the low
 323 Q^2 and high x region $x > 0.7$ since this region is very difficult to model theoretically due
 324 to the presence of target mass corrections, large x resummation, nuclear off-shell effects
 325 and Fermi motion effects which steeply rise the parton densities when approaching $x = 1$.

326 The PDF uncertainties are determined using the Hessian matrix approach. The
 327 main idea of the Hessian method is that the distribution of the $\chi^2(\{a_i\})$ around its
 328 minimum $\chi^2(\{a_i^0\})$ can be approximately parameterized by a quadratic function of the
 329 n fitting parameters $\{a_i\}$ as $\chi^2(\{a_i\}) \approx \chi^2(\{a_i^0\}) + \sum_{i,j} y_i H_{i,j} y_j$ where $y_i = a_i - a_i^0$ and $H_{i,j} =$
 330 $(1/2)(d^2\chi^2/dy_i dy_j)_{a_i=a_i^0}$ is the Hessian matrix that encodes the impact of variations
 331 around each parameter. Since $H_{i,j}$ is a symmetric matrix, it has n orthogonal eigenvectors.
 332 The eigenvectors of $H_{i,j}$ are used to define a new basis $\{z_k\}$ which transform H into a
 333 diagonal matrix. In order to compute the PDF uncertainties, the EPPS16 and nCTEQ15
 334 calculations provide the PDF central set S_0 and the PDF error sets S_k^\pm defined in the $\{z_k\}$
 335 coordinates. Each S_k^\pm is determined by evaluating the PDF on $\{z_k^\pm\}$ defined by varying
 336 upward/downward the parameter $\{z_k\}$ along the k -th eigenvector direction as:

$$S_k^\pm = f\left(z_k^0 \pm \sqrt{\frac{\Delta\chi^2}{\lambda_k}}\right) \quad (3.15)$$

337 where λ_k is the k -th eigenvalue of H and $\Delta\chi^2$ is the tolerance criterion defined at
 338 90% confidence limit. In nCTEQ15 the tolerance is set to $\Delta\chi^2 = 35$ while in EPPS16 it is
 339 set to $\Delta\chi^2 = ??$. Using the PDF error sets, the PDF uncertainties can then be defined as:

$$\Delta O = \sqrt{\sum_i [\max_{\min} \{O(S_i^+) - O(S_i^0), O(S_i^-) - O(S_i^0), 0\}]^2} \quad (3.16)$$

340 To derive the correlation between two observables X and Y , one can use the cosine of
 341 the correlation angle define as:

$$\cos\phi[X, Y] = \frac{\sum_{i_{\text{PDF}}} (X_{i_{\text{PDF}}}^+ - X_{i_{\text{PDF}}}^-)}{(Y_{i_{\text{PDF}}}^+ - Y_{i_{\text{PDF}}}^-)} \sqrt{\sum_{j_{\text{PDF}}} (X_{j_{\text{PDF}}}^+ - X_{j_{\text{PDF}}}^-)^2} \sqrt{\sum_{k_{\text{PDF}}} (Y_{k_{\text{PDF}}}^+ - Y_{k_{\text{PDF}}}^-)^2} \quad (3.17)$$

where the observables are calculated over the upward/downward PDF error sets in each eigenvector direction (16 for nCTEQ15 and 20 for EPPS16). The main differences between the EPS09, EPPS16 and nCTEQ15 nuclear PDFs are summarized in Table 3.1.4.

nPDF	EPS09	EPPS16	nCTEQ15
Order	NLO	NLO	NLO
Fit	nuclear modification	nuclear modification	nuclear PDF
Baseline PDF	CT14	CTEQ6	
Free parameters	15	20	17
Data points	929	1811	708
EMC DY dileptons in p-A	Yes	Yes	Yes
RHIC pions in d-A	Yes	Yes	Yes
SLAC l^\pm -A DIS	Yes	Yes	Yes
CHORUS ν -A DIS	No	Yes	No
RHIC DY in π -A	No	Yes	No
LHC dijets in pPb	No	Yes	No
LHC weak bosons in pPb	No	Yes	No

Table 3.2: Summary of the information of EPS09, EPPS16 and nCTEQ15 nuclear PDFs.

3.1.5 Production of W bosons at LHC

The production of W bosons in hadronic collisions is accomplished through the process of quark-antiquark annihilation. The measurement of W boson production in pPb collisions at $\sqrt{s_{\text{NN}}} = 8.16$ TeV is performed in the semimuonic decay channel. At leading order (LO), the W boson hadroproduction to final state leptons is described by the Feynman diagram shown in Fig. 3.5.

In this thesis, the cross section of the W boson production is measured in pPb collisions as a function of muon pseudorapidity (η) considering muons with p_{T} larger than 25 GeV/c. The theoretical cross section can be derived using electroweak theory and the factorization theorem shown in Eq. (3.8). The W boson hadroproduction cross section has been calculated in Ref. [57], and the corresponding pPb LO differential cross section as a function of muon η , considering $\Gamma_{\text{W}} \ll M_{\text{W}}$, is:

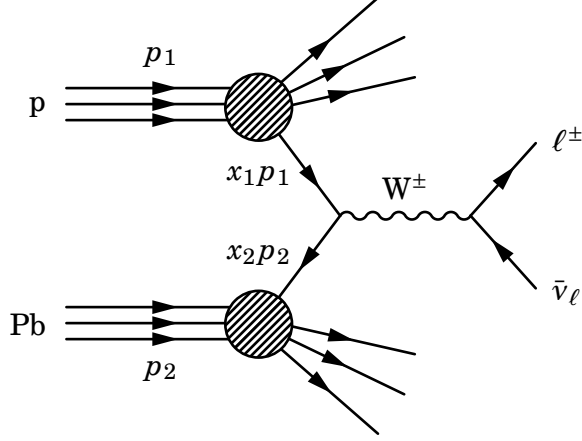


Figure 3.5: Feynman diagram of LO W boson production to final state leptons in pPb collisions

$$\begin{aligned}
 \frac{d\sigma^{W^\pm}}{d\eta}(s_{NN}) \approx & \frac{\pi^2}{6M_W^5 \Gamma_W} \left(\frac{\alpha_{em}}{\sin^2(\theta_W)} \right)^2 \int_{25}^{\text{inf}} dp_T \frac{p_T^3}{\sqrt{1 - 4p_T^2/M_W^2}} \sum_{i,j} \delta(e_{q_i} + e_{\bar{q}_j}, \pm 1) |V_{ij}^{\text{CKM}}|^2 \\
 & \left\{ x_p^\pm q_i^p(x_p^+, Q^2) \cdot x_{Pb}^\mp \bar{q}_j^{Pb}(x_{Pb}^+, Q^2) + x_p^\pm \bar{q}_i^p(x_p^-, Q^2) \cdot x_{Pb}^\mp q_j^{Pb}(x_{Pb}^-, Q^2) + \right. \\
 & \left. x_p^\mp q_i^p(x_p^-, Q^2) \cdot x_{Pb}^\pm \bar{q}_j^{Pb}(x_{Pb}^-, Q^2) + x_p^\mp \bar{q}_i^p(x_p^+, Q^2) \cdot x_{Pb}^\pm q_j^{Pb}(x_{Pb}^+, Q^2) \right\}
 \end{aligned} \tag{3.18}$$

where α_{em} is the fine-structure constant, q^p is the free-proton quark PDF, q_i^{Pb} is the Pb nuclear quark PDF, and $Q \approx M_W$ is the momentum scale. The sum in Eq. (3.18) is performed over all quark flavours and the parton momentum fraction variables x_p and x_{Pb} are defined as [57]:

$$\begin{aligned}
 x_p^\pm &= \frac{M_W}{\sqrt{s_{NN}}} e^\eta \left[\frac{1 \mp \sqrt{1 - 4p_T^2/M_W^2}}{2p_T/M_W} \right] \\
 x_{Pb}^\pm &= \frac{M_W}{\sqrt{s_{NN}}} e^{-\eta} \left[\frac{1 \pm \sqrt{1 - 4p_T^2/M_W^2}}{2p_T/M_W} \right]
 \end{aligned} \tag{3.19}$$

The cross sections of negative and positive charged leptons, shown in Eq. (3.18), are different due to parity violation and helicity conservation of weak decays. Since W^+ bosons couple to right-handed leptons while W^- couples to left-handed leptons, leptons

are produced in the same direction as the W boson while antileptons are generated in the opposite direction. This is reflected in Eq. (3.19) where μ^- production is sensitive to slightly higher x than μ^+ production.

Multiple proton-proton and proton-neutron hard scatterings takes place during pPb collisions. In this case, the W bosons are mainly produced from interactions between the valence quarks and sea antiquarks of the nucleons. The dominant production modes of W^+ bosons correspond to up quark and down antiquark annihilation while for W^- bosons correspond to down quark and up antiquark annihilation. The annihilation between light quarks and heavier antiquarks is also possible but highly suppressed according to the CKM matrix elements. Therefore, the inclusive W boson cross section measured in pPb data is mostly sensitive to the proton and Pb-nucleus PDFs of light quarks and antiquarks.

In addition, the W boson cross sections can be compared between different beam energies. According to Arleo and Chapon [57], at small enough x values, the W boson cross section follows a power-like scaling as a function of s_{NN} , where Eq. (3.18) can be approximately reduced to:

$$\begin{aligned} \frac{d\sigma^{W^\pm}}{d\eta}(s_{NN}, \xi_p) &\approx (s_{NN})^\alpha \times F_{p, Pb}^\pm(\xi_p, p_T), \quad \eta >> 0, \\ \frac{d\sigma^{W^\pm}}{d\eta}(s_{NN}, \xi_{Pb}) &\approx (s_{NN})^\alpha \times G_{p, Pb}^\pm(\xi_{Pb}, p_T), \quad \eta << 0 \end{aligned} \quad (3.20)$$

where α is the scaling parameter, and $\xi_p = (M_W/\sqrt{s_{NN}})e^{-\eta}$ and $\xi_{Pb} = (M_W/\sqrt{s_{NN}})e^\eta$ are the x values at $p_T = M_W/2$ in the proton and Pb ion, respectively. Moreover, the functions $F_{p, Pb}^\pm$ and $G_{p, Pb}^\pm$ do not depend explicitly on s or η .

Furthermore, since the scaling parameter does not depend on the lepton pseudorapidity or the charge of the W boson, the dependence on s_{NN} cancels in ratios of W boson cross sections. We can then measure asymmetries to improve the sensitivity to different aspects of the W boson production. Two of the most commonly used are the lepton charge asymmetry defined in Eq. (3.22) and the forward-backward ratio presented in Eq. (3.24). Thus, according to Eq. (3.20), the W boson asymmetries only depends on ξ_p and ξ_{Pb} for $|\eta| >> 0$.

3.2 W boson production in pPb collisions at

$$\sqrt{s_{\text{NN}}} = 8.16 \text{ TeV}$$

This section presents the results of the analysis of the production of W bosons in pPb collisions at $\sqrt{s_{\text{NN}}} = 8.16 \text{ TeV}$ performed in the semi-muonic decay channel, using a data sample with integrated luminosity of $173.4 \pm 5.9 \text{ nb}^{-1}$ [58]. The W boson yields are extracted in the muon kinematic region defined by $p_{\text{T}}^{\mu} > 25 \text{ GeV}/c$ and $|\eta_{\text{lab}}^{\mu}| < 2.4$. The W boson differential cross sections, the muon charge asymmetry, and the muon forward-backward ratios are measured as a function of muon η_{CM} . The measurements are compared to PDF calculations both without and with including nuclear modifications, and also to results from other LHC experiments.

3.2.1 Observables

3.2.1.1 W boson cross sections

The differential $W \rightarrow \mu\nu_{\mu}$ cross sections are calculated by dividing the efficiency-corrected $W \rightarrow \mu\nu_{\mu}$ yields (N_{corr}) over the recorded integrated luminosity (\mathcal{L}) times the bin width ($\Delta\eta_{\text{CM}}$), as described below:

$$\frac{d\sigma^{\pm}}{d\eta_{\text{CM}}}(\eta_{\text{CM}}) = \frac{N_{\text{corr}}^{\pm}(\eta_{\text{CM}})}{\Delta\eta_{\text{CM}}\mathcal{L}} \quad (3.21)$$

The results of the production cross sections for $W^{+} \rightarrow \mu^{+}\nu_{\mu}$ and $W^{-} \rightarrow \mu^{-}\bar{\nu}_{\mu}$, as a function muon η_{CM} , are shown in Fig. 3.6. The vertical error bars represent the statistical uncertainties from the measured $W \rightarrow \mu\nu_{\mu}$ yields, while the brackets show the statistical and total systematic uncertainties summed in quadrature. The global integrated luminosity uncertainty of $\pm 3.4\%$ [58] is not shown.

The opposite trend seen between the W^{+} and W^{-} boson differential cross sections is expected from parity violation of the electroweak interaction. The W^{+} bosons decay to a right-handed antimuon boosted in the opposite direction, while the W^{-} bosons decay to a left-handed muon along the direction of the W^{-} boson. As a consequence, the μ^{+} and μ^{-} yields differ as a function of the muon η_{CM} .

3.2.1.2 Muon charge asymmetry

The muon charge asymmetry (C_{μ}) between $W^{-} \rightarrow \mu^{-}\bar{\nu}_{\mu}$ and $W^{+} \rightarrow \mu^{+}\nu_{\mu}$ processes and its corresponding uncertainty are defined in Eq. (3.22) and Eq. (3.23), respectively.

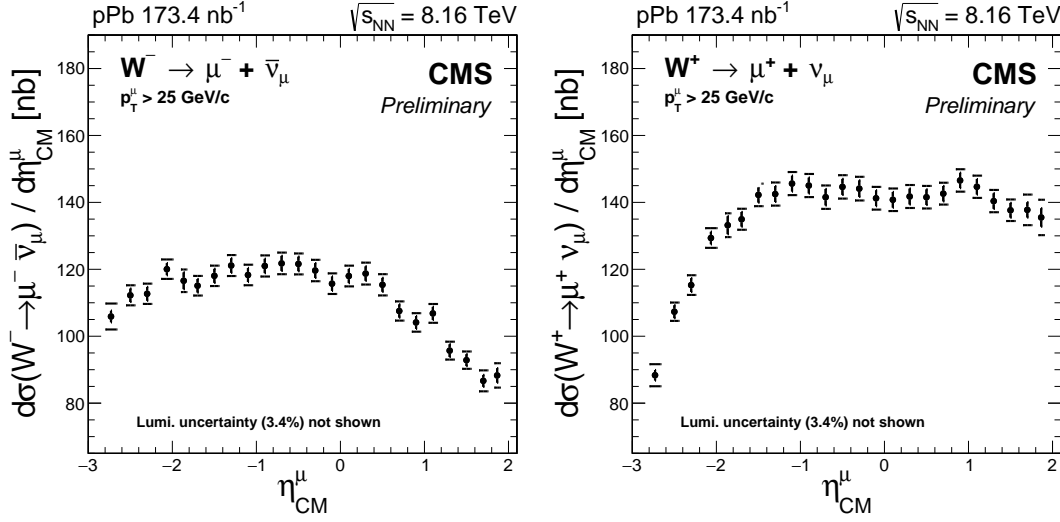


Figure 3.6: Production cross sections for $W^+ \rightarrow \mu^+ \nu_\mu$ (left) and $W^- \rightarrow \mu^- \bar{\nu}_\mu$ (right), as a function of the muon pseudorapidity in the center-of-mass frame. The brackets represent the statistical and systematic uncertainties summed in quadrature, while the error bars show the statistical uncertainties only. The global luminosity uncertainty of $\pm 3.4\%$ [58] is not shown.

$$C_\mu(\eta_{CM}) = \frac{N_{corr}^+(\eta_{CM}) - N_{corr}^-(\eta_{CM})}{N_{corr}^+(\eta_{CM}) + N_{corr}^-(\eta_{CM})} \quad (3.22)$$

$$\delta C_\mu(\eta_{CM}) = \left(\frac{2 \times N_{corr}^+(\eta_{CM}) \times N_{corr}^-(\eta_{CM})}{(N_{corr}^+(\eta_{CM}) + N_{corr}^-(\eta_{CM}))^2} \right) \times \sqrt{\left(\frac{\delta N_{corr}^+(\eta_{CM})}{N_{corr}^+(\eta_{CM})} \right)^2 + \left(\frac{\delta N_{corr}^-(\eta_{CM})}{N_{corr}^-(\eta_{CM})} \right)^2} \quad (3.23)$$

418 The uncertainties correlated in muon charge, such as the integrated luminosity
 419 uncertainty of 3.4% and the systematic components of the tag-and-probe correction
 420 uncertainties ($< 2.8\%$), cancel in the measurement of the muon charge asymmetry. The
 421 measured muon charge asymmetry is shown in Fig. 3.7 as a function muon η_{CM} .

422 3.2.1.3 Muon forward-backward ratios

423 The muon forward-backward ratio (R_{FB}) is defined as the ratio of the $W \rightarrow \mu \nu_\mu$ yields
 424 extracted in the forward η_{CM} bin divided by its backward counterpart. By convention,
 425 the forward region corresponds to the proton-going direction while the backward region
 426 corresponds to the Pb-going direction. The muon forward-backward ratio is measured
 427 for each muon charge separately, and also considering all muons. The R_{FB} is defined in
 428 Eq. (3.24) and its uncertainty is computed using Eq. (3.25).

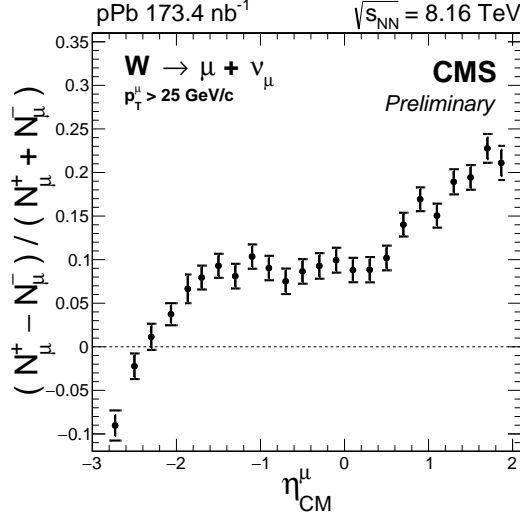


Figure 3.7: Muon charge asymmetry as a function of the muon pseudorapidity in the center-of-mass frame. The brackets represent the statistical and systematic uncertainties summed in quadrature, while the error bars show the statistical uncertainties only.

$$R_{FB}(\eta) = \frac{N_{corr}(+\eta_{CM})}{N_{corr}(-\eta_{CM})} \quad (3.24)$$

$$\delta R_{FB}(\eta_{CM}) = R_{FB}(\eta_{CM}) \times \sqrt{\left(\frac{\delta N_{corr}(+\eta_{CM})}{N_{corr}(+\eta_{CM})}\right)^2 + \left(\frac{\delta N_{corr}(-\eta_{CM})}{N_{corr}(-\eta_{CM})}\right)^2} \quad (3.25)$$

429 The results of the forward-backward ratio of all muons and the ratio for $W^- \rightarrow$
 430 $\mu^- \bar{\nu}_\mu$ and $W^+ \rightarrow \mu^+ \nu_\mu$ decays, are shown in Fig. 3.8. The uncertainties correlated in
 431 muon pseudorapidity, such as the integrated luminosity uncertainty of 3.4%, the event
 432 activity reweighing uncertainty and the systematic uncertainties due to the electroweak
 433 backgrounds, are strongly reduced.

434 3.2.2 Comparison with theoretical models

435 The measurements of the W boson production in pPb collisions at $\sqrt{s_{NN}} = 8.16$ TeV
 436 are compared to three NLO PDF calculations, one assuming no nuclear effects (CT14
 437 PDF [50]) and two including nuclear modifications (CT14+EPPS16 nPDF [56] and
 438 CT14+nCTEQ15 nPDF [55]). The NLO PDF calculations are produced using the parton-
 439 level Monte Carlo program MCFM [59]. The comparison between the PDF calculations
 440 and the data are shown in Fig. 3.9 for the W differential cross sections, in Fig. 3.10 for
 441 the muon charge asymmetry and in Fig. 3.11 for the muon forward backward ratios.

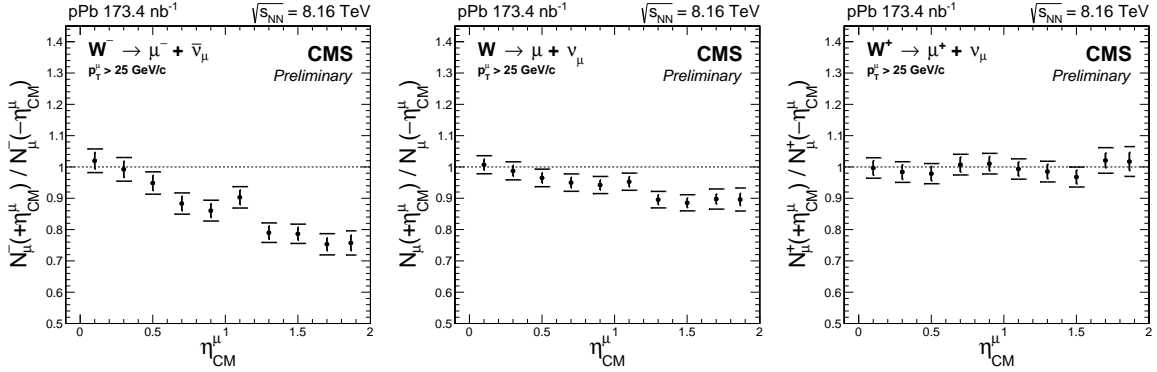


Figure 3.8: Forward-backward ratios, for the positive (left), all (middle) and negative (right) charged muons. The brackets represent the statistical and systematic uncertainties summed in quadrature, while the error bars show the statistical uncertainties only.

In all cases, the PDF calculations with (without) including nuclear modifications are displayed using dashed (continuous) lines and the corresponding PDF uncertainties are shown using hatched (filled) boxes.

As can be seen in Fig. 3.9, the W cross section measurements at forward rapidity favor the PDF calculations including nuclear modifications, while at backward rapidity all three PDF calculations are in good agreement with the data. Moreover, in the case of the muon charge asymmetry shown in Fig. 3.10, the results of the theory calculations derived using CT14 PDF only, and those including nuclear modifications described by EPPS16 nPDF, are in good agreement with the measurements while the CT14+nCTEQ15 nPDF calculations expect a slightly larger muon charge asymmetry in the most backward η_{CM} bins. Finally, from the ratios of muon yields at forward over backward η_{CM} displayed in Fig. 3.11, the nuclear PDF calculations describe much better the data compared to the free-nucleon PDF calculation. Considering the smaller size of the uncertainties compared to the theory uncertainties, the measurements have the potential to constrain the CT14+EPPS16 and the CT14+nCTEQ15 nPDF models.

In order to quantify the level of agreement between each PDF calculation and the measurements of the W boson production in pPb, a χ^2 test is performed. The χ^2 test is derived as described below:

$$\chi^2 = \sum_i \sum_j \left[(t(i) - d(i)) (cov_{data} + cov_{theory})^{-1} [i, j] (t(j) - d(j)) \right] \quad (3.26)$$

where $t(i)$ is the value of the observable predicted from the PDF calculation in bin i ,

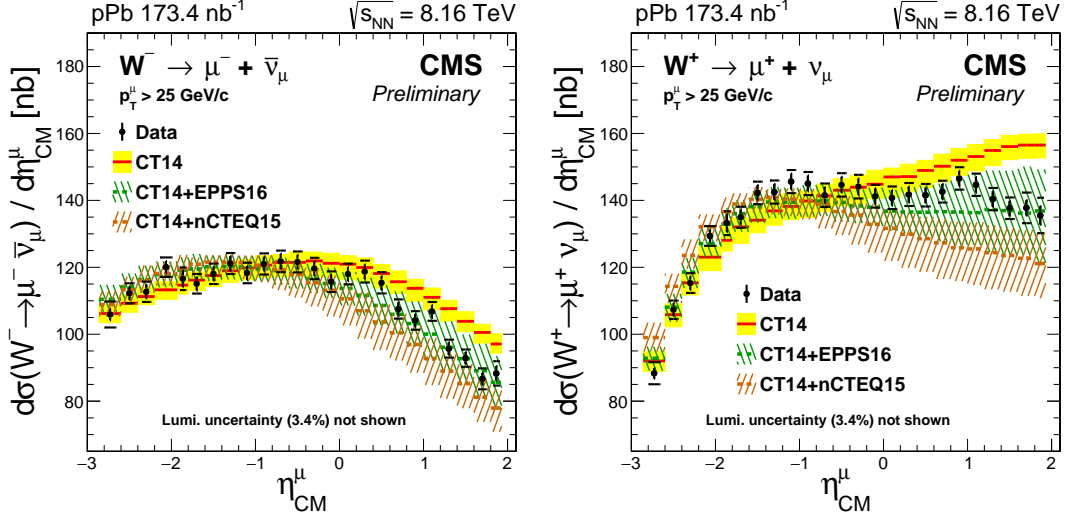


Figure 3.9: Differential cross sections for $W^+ \rightarrow \mu^+ \nu_\mu$ (left) and $W^- \rightarrow \mu^- \bar{\nu}_\mu$ (right), as a function of the muon pseudorapidity in the center-of-mass frame. Errors bars represent the statistical uncertainties, while the brackets represent the statistical and systematic uncertainties summed in quadrature. The global luminosity uncertainty of $\pm 3.4\%$ is not displayed. Theoretical predictions with (CT14+EPSS16 shown in dashed green line and CT14+nCTEQ15 shown in dashed brown line) and without (CT14, solid red line) PDF nuclear modifications are also shown, with the uncertainty bands. All theory uncertainty bands include PDF uncertainties.

461 $d(i)$ is the value of the observable measured in data in bin i , and $(cov_{data} + cov_{theory})^{-1}$
 462 is the inverse of the sum of the covariance matrices extracted from the data and the
 463 model. This approach takes into account the bin-to-bin correlations in both muon charge
 464 and pseudorapidity. The outcome of the χ^2 statistical test derived using the CT14 PDF,
 465 the CT14+EPSS16 nPDF and the CT14+nCTEQ15 nPDF calculations are summarized
 466 in Table 3.3.

3.2.3 Comparison with other LHC experiments

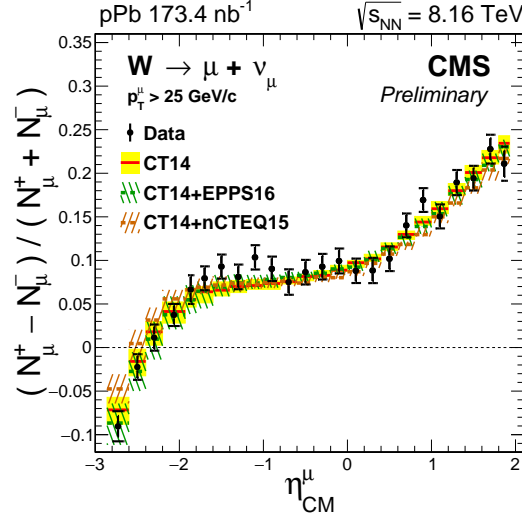


Figure 3.10: Muon charge asymmetry of $W \rightarrow \mu\nu_\mu$, given for each muon η_{CM} bin. Errors bars represent the statistical uncertainties, while the brackets represent the statistical and systematic uncertainties summed in quadrature. Theoretical predictions with (CT14+EPPS16 shown in dashed green line and CT14+nCTEQ15 shown in dashed brown line) and without (CT14, solid red line) PDF nuclear modifications are also shown, with the uncertainty bands. All theory uncertainty bands include PDF uncertainties.

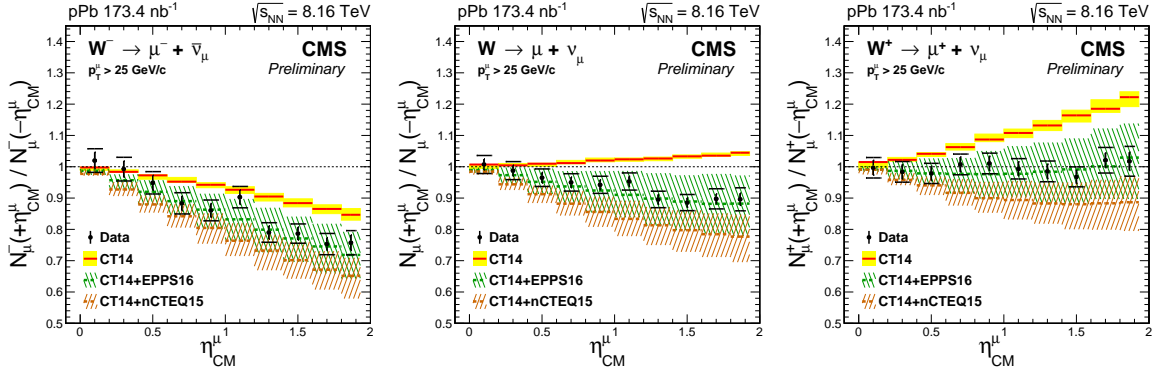


Figure 3.11: Forward-backward ratio of $W \rightarrow \mu\nu_\mu$, given for each muon η_{CM} bin separated in negative (left), all (middle) and positive (right) charged muons. Errors bars represent the statistical uncertainties, while the brackets represent the statistical and systematic uncertainties summed in quadrature. Theoretical predictions with (CT14+EPPS16 shown in dashed green line and CT14+nCTEQ15 shown in dashed brown line) and without (CT14, solid red line) PDF nuclear modifications are also shown, with the uncertainty bands. All theory uncertainty bands include PDF uncertainties.

Observable	CT14			CT14+EPPS16			CT14+nCTEQ15		
	χ^2	ndf	Prob.(%)	χ^2	ndf	Prob.(%)	χ^2	ndf	Prob.(%)
$d\sigma(W \rightarrow \mu\nu_\mu)/d\eta_{CM}^\mu$	136	48	0	32	48	96	40	48	79
$(N_\mu^+ - N_\mu^-)/(N_\mu^+ + N_\mu^-)$	23	24	54	18	24	80	29	24	23
$N_\mu^\pm(+\eta_{CM}^\mu)/N_\mu^\pm(-\eta_{CM}^\mu)$	98	20	0	11	20	95	14	20	83
$N_\mu(+\eta_{CM}^\mu)/N_\mu(-\eta_{CM}^\mu)$	87	10	0	3	10	99	5	10	90

Table 3.3: Results of the χ^2 statistical test between the measurements and the theory calculations from the CT14 PDF, CT14+EPPS16 nPDF and CT14+nCTEQ15 nPDF models. The value of the χ^2 , the number of degrees of freedom (ndf) and the χ^2 probability (Prob.), are presented for the W differential cross sections, the muon charge asymmetry, the charged muon forward-backward ratios, and the forward-backward ratio of all muons, respectively.

CHAPTER



CONCLUSION

BIBLIOGRAPHY

- [1] **CMS** Collaboration, V. Khachatryan *et al.*, “Study of W boson production in pPb collisions at $\sqrt{s_{\text{NN}}} = 5.02$ TeV”, *Phys. Lett.* **B750** (2015) 565–586, arXiv:1503.05825. [[Cited on page 5.](#)]
- [2] **ALICE** Collaboration, K. Senosi, “Measurement of W-boson production in p-Pb collisions at the LHC with ALICE”, *PoS Bormio2015* (2015) 042, arXiv:1511.06398. [[Cited on page 5.](#)]
- [3] **ATLAS** Collaboration, M. Dumanfçifá, “W and Z boson production in 5.02 TeV pp and p +Pb collisions with the ATLAS detector”, *Nucl. Part. Phys. Proc.* **289-290** (2017) 193–196, arXiv:1704.00298. [[Cited on page 5.](#)]
- [4] E. Rutherford, “Uranium radiation and the electrical conduction produced by it”, *Philos. Mag.* **47** (1899) 109. [[Cited on page 6.](#)]
- [5] J. Chadwick, “Intensitätsverteilung im magnetischen Spektrum von β -Strahlen von Radium B+C”, *Verhandlungen der deutschen physikalischen Gesellschaft* **16** (1914) 383. [[Cited on page 6.](#)]
- [6] J. Chadwick and C. D. Ellis, “A Preliminary Investigation of the Intensity Distribution in the β -Ray Spectra of Radium B and C”, *Proceedings of the Cambridge Philosophical Society* **21** (1922) 274. [[Cited on page 6.](#)]
- [7] W. Pauli, “Fünf Arbeiten zum Ausschliessungsprinzip und zum Neutrino”, Wissenschaftliche Buchgesellschaft, [Abt. Verlag], 1977. [[Cited on page 6.](#)]
- [8] K. Winter, “Neutrino physics”, Cambridge University Press, 1991. [[Cited on page 6.](#)]
- [9] J. Chadwick, “Possible Existence of a Neutron”, *Nature* **129** (1932) 312. [[Cited on page 6.](#)]

- [10] E. Fermi, “Collected Papers of Enrico Fermi”, University of Chicago Press, 1965.
[Cited on page 6.]
- [11] E. Fermi, “Versuch einer Theorie der β -Strahlen. I”, *Zeitschrift für Physik* **88** (1934) 161. [Cited on page 6.]
- [12] T. D. Lee and C. N. Yang, “Question of Parity Conservation in Weak Interactions”, *Phys. Rev.* **104** (1956) 254. [Cited on page 7.]
- [13] C. S. Wu, E. Ambler, R. W. Hayward, D. D. Hoppes, and R. P. Hudson, “Experimental Test of Parity Conservation in Beta Decay”, *Phys. Rev.* **105** (1957) 1413. [Cited on page 7.]
- [14] M. Goldhaber, L. Grodzins, and A. W. Sunyar, “Helicity of Neutrinos”, *Phys. Rev.* **109** (1958) 1015. [Cited on page 7.]
- [15] J. H. Christenson, J. W. Cronin, V. L. Fitch, and R. Turlay, “Evidence for the 2π Decay of the K_2^0 Meson”, *Phys. Rev. Lett.* **13** (1964) 138–140. [Cited on page 7.]
- [16] M. Kobayashi and T. Maskawa, “CP Violation in the Renormalizable Theory of Weak Interaction”, *Prog. Theor. Phys.* **49** (1973) 652–657. [Cited on page 7.]
- [17] N. Cabibbo, “Unitary Symmetry and Leptonic Decays”, *Phys. Rev. Lett.* **10** (1963) 531–533, [,648(1963)]. [Cited on page 7.]
- [18] S. W. Herb *et al.*, “Observation of a Dimuon Resonance at 9.5-GeV in 400-GeV Proton-Nucleus Collisions”, *Phys. Rev. Lett.* **39** (1977) 252–255. [Cited on page 7.]
- [19] **CDF** Collaboration, F. Abe *et al.*, “Observation of top quark production in $\bar{p}p$ collisions”, *Phys. Rev. Lett.* **74** (1995) 2626–2631, arXiv:hep-ex/9503002. [Cited on page 7.]
- [20] P. A. M. Dirac, “The Principles of Quantum Mechanics”, Clarendon Press, 1930. [Cited on page 7.]
- [21] S. L. Glashow, “The renormalizability of vector meson interactions”, *Nucl. Phys.* **10** (1959) 107. [Cited on pages 7 and 9.]
- [22] S. Weinberg, “A Model of Leptons”, *Phys. Rev. Lett.* **19** (1967) 1264. [Cited on page 7.]

- [23] A. Salam, “Weak and Electromagnetic Interactions”, *Conf. Proc. C* **680519** (1968) 367. [[Cited on pages 7 and 9.](#)]
- [24] N. M. A. 2014, “The Nobel Prize in Physics 1979”.
http://www.nobelprize.org/nobel_prizes/physics/laureates/1979/, 2018.
Accessed: 2018-05-23. [[Cited on page 8.](#)]
- [25] P. W. Higgs, “Broken Symmetries and the Masses of Gauge Bosons”, *Phys. Rev. Lett.* **13** (1964) 367. [[Cited on pages 8 and 9.](#)]
- [26] F. Englert and R. Brout, “Broken Symmetry and the Mass of Gauge Vector Mesons”, *Phys. Rev. Lett.* **13** (1964) 321. [[Cited on pages 8 and 9.](#)]
- [27] G. t. Hooft, “Renormalizable Lagrangians for massive Yang-Mills fields”, *Nuclear Physics B* **35** (1971) 167. [[Cited on page 8.](#)]
- [28] G. t. Hooft and M. Veltman, “Regularization and renormalization of gauge fields”, *Nuclear Physics B* **44** (1972) 189. [[Cited on page 8.](#)]
- [29] C. Rubbia, P. McIntyre, and D. Cline, *Producing Massive Neutral Intermediate Vector Bosons with Existing Accelerators*, pp. 683–687. Vieweg+Teubner Verlag, Wiesbaden, 1977. [[Cited on page 8.](#)]
- [30] S. van der Meer, “Stochastic damping of betatron oscillations in the ISR”, Tech. Rep. CERN-ISR-PO-72-31. ISR-PO-72-31, CERN, Geneva, Aug 1972. [[Cited on page 8.](#)]
- [31] G. Arnison *et al.*, “Experimental observation of isolated large transverse energy electrons with associated missing energy at $\sqrt{s}=540$ GeV”, *Phys. Lett. B* **122** (1983) 103. [[Cited on page 8.](#)]
- [32] M. Banner *et al.*, “Observation of single isolated electrons of high transverse momentum in events with missing transverse energy at the CERN pp collider”, *Phys. Lett. B* **122** (1983) 476. [[Cited on page 8.](#)]
- [33] UA1 Collaboration, G. Arnison *et al.*, “Experimental Observation of Lepton Pairs of Invariant Mass Around 95-GeV/c**2 at the CERN SPS Collider”, *Phys. Lett. B* **126** (1983) 398, [,7.55(1983)]. [[Cited on page 8.](#)]
- [34] UA2 Collaboration, P. Bagnaia *et al.*, “Evidence for $Z^0 \rightarrow e^+ e^-$ at the CERN anti-p p Collider”, *Phys. Lett. B* **129** (1983) 130, [,7.69(1983)]. [[Cited on page 8.](#)]

- [35] N. M. A. 2014, “The Nobel Prize in Physics 1984”.
http://www.nobelprize.org/nobel_prizes/physics/laureates/1984/, 2018.
Accessed: 2018-05-23. [Cited on page 8.]
- [36] S. Myers, “The LEP Collider, from design to approval and commissioning”, CERN, Geneva, 1991. Delivered at CERN, 26 Nov 1990. [Cited on page 8.]
- [37] **DØ Collaboration** Collaboration, V. M. Abazov *et al.*, “Improved W boson mass measurement with the DØ detector”, *Phys. Rev. D* **66** Jul (2002) 012001. [Cited on page 8.]
- [38] R. R. Wilson, “The Tevatron”, *Phys. Today* **30** (1977) 23. [Cited on page 8.]
- [39] **CMS Collaboration**, S. Chatrchyan *et al.*, “Observation of a new boson at a mass of 125 GeV with the CMS experiment at the LHC”, *Phys. Lett. B* **716** (2012) 30, arXiv:1207.7235. [Cited on page 8.]
- [40] **ATLAS Collaboration**, G. Aad *et al.*, “Observation of a new particle in the search for the Standard Model Higgs boson with the ATLAS detector at the LHC”, *Phys. Lett. B* **716** (2012) 1, arXiv:1207.7214. [Cited on page 8.]
- [41] **Particle Data Group** Collaboration, C. Patrignani *et al.*, “Review of Particle Physics”, *Chin. Phys.* **C40** (2016), no. 10, 100001. [Cited on pages 10, 11, and 37.]
- [42] J. D. Bjorken, “CURRENT ALGEBRA AT SMALL DISTANCES”, *Conf. Proc.* **670717** (1967) 55–81. [Cited on page 12.]
- [43] G. Altarelli and G. Parisi, “Asymptotic Freedom in Parton Language”, *Nucl. Phys. B* **126** (1977) 298–318. [Cited on page 12.]
- [44] Y. L. Dokshitzer, “Calculation of the Structure Functions for Deep Inelastic Scattering and e^+e^- Annihilation by Perturbation Theory in Quantum Chromodynamics.”, *Sov. Phys. JETP* **46** (1977) 641–653, [Zh. Eksp. Teor. Fiz.73,1216(1977)]. [Not cited.]
- [45] V. N. Gribov and L. N. Lipatov, “Deep inelastic $e p$ scattering in perturbation theory”, *Sov. J. Nucl. Phys.* **15** (1972) 438–450, [Yad. Fiz.15,781(1972)]. [Cited on page 12.]

- [46] **ZEUS** Collaboration, S. Chekanov *et al.*, “A ZEUS next-to-leading-order QCD analysis of data on deep inelastic scattering”, *Phys. Rev.* **D67** (2003) 012007, arXiv:hep-ex/0208023. [Cited on pages 13, 14, and 39.]
- [47] **European Muon** Collaboration, J. J. Aubert *et al.*, “The ratio of the nucleon structure functions $F2_n$ for iron and deuterium”, *Phys. Lett. B* **123** (1983) 275–278. [Cited on page 15.]
- [48] **European Muon** Collaboration, M. Arneodo *et al.*, “Shadowing in Deep Inelastic Muon Scattering from Nuclear Targets”, *Phys. Lett. B* **211** (1988) 493–499. [Cited on page 15.]
- [49] **New Muon** Collaboration, D. o. Allasia, “Inelastic j/ψ production in deep inelastic scattering from hydrogen and deuterium and the gluon distribution of free nucleons”, *Physics Letters B* **258** (1991), no. 3, 493 – 498. [Cited on page 15.]
- [50] S. Dulat, T.-J. Hou, J. Gao, M. Guzzi, J. Huston, P. Nadolsky, J. Pumplin, C. Schmidt, D. Stump, and C. P. Yuan, “New parton distribution functions from a global analysis of quantum chromodynamics”, *Phys. Rev.* **D93** (2016), no. 3, 033006, arXiv:1506.07443. [Cited on pages 16 and 24.]
- [51] K. J. Eskola, V. J. Kolhinen, and C. A. Salgado, “The Scale dependent nuclear effects in parton distributions for practical applications”, *Eur. Phys. J. C* **9** (1999) 61–68, arXiv:hep-ph/9807297. [Cited on page 16.]
- [52] K. J. Eskola, H. Paukkunen, and C. A. Salgado, “An Improved global analysis of nuclear parton distribution functions including RHIC data”, *JHEP* **07** (2008) 102, arXiv:0802.0139. [Cited on page 16.]
- [53] K. J. Eskola, H. Paukkunen, and C. A. Salgado, “EPS09: A new generation of NLO and LO nuclear parton distribution functions”, *JHEP* **04** (2009) 065, arXiv:0902.4154. [Cited on page 16.]
- [54] D. de Florian, R. Sassot, P. Zurita, and M. Stratmann, “Global Analysis of Nuclear Parton Distributions”, *Phys. Rev. D* **85** (2012) 074028, arXiv:1112.6324. [Cited on page 16.]
- [55] K. Kovarik *et al.*, “nCTEQ15 - Global analysis of nuclear parton distributions with uncertainties in the CTEQ framework”, *Phys. Rev. D* **93** (2016), no. 8, 085037, arXiv:1509.00792. [Cited on pages 16 and 24.]

- [56] K. J. Eskola, P. Paakkinen, H. Paukkunen, and C. A. Salgado, “EPPS16: Nuclear parton distributions with LHC data”, *Eur. Phys. J. C* **77** (2017), no. 3, 163, arXiv:1612.05741. [Cited on pages 16 and 24.]
- [57] F. Arleo, É. Chapon, and H. Paukkunen, “Scaling properties of inclusive W^\pm production at hadron colliders”, *Eur. Phys. J. C* **76** (2016), no. 4, 214, arXiv:1509.03993. [Cited on pages 19, 20, and 21.]
- [58] **CMS Collaboration** Collaboration, “Luminosity calibration for the pPb/Pbp 2016 runs”, Tech. Rep. CMS-LUM-AN-17-002, CERN, Geneva, 2017. [Cited on pages 22, 23, and 39.]
- [59] J. M. Campbell and R. K. Ellis, “MCFM for the Tevatron and the LHC”, *Nucl. Phys. Proc. Suppl.* **205-206** (2010) 10–15, arXiv:1007.3492. [Cited on page 24.]

LIST OF TABLES

3.1	Experimental values of the mass, width and branching fractions of weak bosons extracted from the PDG [41].	11
3.2	Summary of the information of EPS09, EPPS16 and nCTEQ15 nuclear PDFs.	19
3.3	Results of the χ^2 statistical test between the measurements and the theory calculations from the CT14 PDF, CT14+EPPS16 nPDF and CT14+nCTEQ15 nPDF models. The value of the χ^2 , the number of degrees of freedom (ndf) and the χ^2 probability (Prob.), are presented for the W differential cross sections, the muon charge asymmetry, the charged muon forward-backward ratios, and the forward-backward ratio of all muons, respectively.	28

TABLE

Page

LIST OF FIGURES

3.1	Feynman diagram of the decay modes of W^+ (left) and W^- (right) bosons to fermions.	11
3.2	NLO QCD fits to the to the ZEUS F_2 structure function data from 1996, 1997 and proton fixed-target at HERA. The error bands of the fit represent the total experimental uncertainty from both correlated and uncorrelated sources. Figure taken from Ref. [46]	14
3.3	Feynman diagram of deep inelastic scattering of electrons against protons . .	14
3.4	Feynman diagram of neutral charged Drell-Yan process	15
3.5	Feynman diagram of LO W boson production to final state leptons in pPb collisions	20
3.6	Production cross sections for $W^+ \rightarrow \mu^+ \nu_\mu$ (left) and $W^- \rightarrow \mu^- \bar{\nu}_\mu$ (right), as a function of the muon pseudorapidity in the center-of-mass frame. The brackets represent the statistical and systematic uncertainties summed in quadrature, while the error bars show the statistical uncertainties only. The global luminosity uncertainty of $\pm 3.4\%$ [58] is not shown.	23
3.7	Muon charge asymmetry as a function of the muon pseudorapidity in the center-of-mass frame. The brackets represent the statistical and systematic uncertainties summed in quadrature, while the error bars show the statistical uncertainties only.	24
3.8	Forward-backward ratios, for the positive (left), all (middle) and negative (right) charged muons. The brackets represent the statistical and systematic uncertainties summed in quadrature, while the error bars show the statistical uncertainties only.	25

3.9	Differential cross sections for $W^+ \rightarrow \mu^+ \nu_\mu$ (left) and $W^- \rightarrow \mu^- \bar{\nu}_\mu$ (right), as a function of the muon pseudorapidity in the center-of-mass frame. Errors bars represent the statistical uncertainties, while the brackets represent the statistical and systematic uncertainties summed in quadrature. The global luminosity uncertainty of $\pm 3.4\%$ is not displayed. Theoretical predictions with (CT14+EPPS16 shown in dashed green line and CT14+nCTEQ15 shown in dashed brown line) and without (CT14, solid red line) PDF nuclear modifications are also shown, with the uncertainty bands. All theory uncertainty bands include PDF uncertainties.	26
3.10	Muon charge asymmetry of $W \rightarrow \mu \nu_\mu$, given for each muon η_{CM} bin. Errors bars represent the statistical uncertainties, while the brackets represent the statistical and systematic uncertainties summed in quadrature. Theoretical predictions with (CT14+EPPS16 shown in dashed green line and CT14+nCTEQ15 shown in dashed brown line) and without (CT14, solid red line) PDF nuclear modifications are also shown, with the uncertainty bands. All theory uncertainty bands include PDF uncertainties.	27
3.11	Forward-backward ratio of $W \rightarrow \mu \nu_\mu$, given for each muon η_{CM} bin separated in negative (left), all (middle) and positive (right) charged muons. Errors bars represent the statistical uncertainties, while the brackets represent the statistical and systematic uncertainties summed in quadrature. Theoretical predictions with (CT14+EPPS16 shown in dashed green line and CT14+nCTEQ15 shown in dashed brown line) and without (CT14, solid red line) PDF nuclear modifications are also shown, with the uncertainty bands. All theory uncertainty bands include PDF uncertainties.	27

FIGURE**Page**